In Situ Sulfur Reduction and Intercalation of Graphite Oxides for Li-S Battery Cathodes

Shiyou Zheng, Yang Wen, Yujie Zhu, Zhuo Han, Jing Wang, Junhe Yang, and Chunsheng Wang**

An increasing number of electric or plug-in hybrid vehicles, portable electronic devices, and power tool technologies require a significant increase of the energy density of Li-ion batteries. Lithium-sulfur (Li-S) batteries have recently attracted more and more attention because they yield a high theoretical specific capacity of 1675 mAh g^{-1}.[1–3] In addition to its high theoretical energy density, S is inexpensive, abundant on earth, and environmentally benign.[4,5] Despite the exceptionally valuable characteristics of the Li–S batteries, the S cathodes suffer from low utilization of the active material and severe capacity fading in an organic liquid electrolyte, which are mainly attributed to the insulating nature of S and dissolution of high-order lithium polysulfide (Li_2S_x, $4 \le x \le 8$) intermediates, and large volume change during lithiation/ delithiation.[6–8]

Extensive research has been conducted to overcome these challenges.[9–13] The most successful technique is the incorporation of S into a porous carbon host.[14] Porous carbon materials with different microstructures and pore sizes have been investigated to improve the conductivity and to protect S from dissolution into liquid electrolytes.[15–19] However, due to the intrinsic insulating nature of S and lithium polysulfides, the dissolution of lithium polysulfides is required for continuous lithiation/delithiation reaction if the S thickness is larger than the electronic tunnel effect size due to a high S loading. Unfortunately, the dissolution of lithium polysulfides will also lead to a shuttle reaction, thus reducing the Coulombic efficiency and cycling stability.

Due to high surface area, high electrical conductivity, and mechanical flexibility, graphene has been used to increase the conductivity of S and protect polysulfide intermediates from dissolution, thus significantly improving cycling stability and Coulombic efficiency of Li-S batteries.[20–22] The graphene-S composite cathodes are normally synthesized using wetting chemical reduction, high-energy ball-milling the mixture of S and edge-opened graphite oxide, chemical reduction of graphene oxide and deposition of S.[23–25] Because the S in these graphene-S composites is not completely encapsulated by graphene, the polysulfide intermediates still slowly dissolve into electrolyte resulting in progressive cycling decay. The ideal structure for the carbon-S composites is to intercalate S atoms or molecules into a graphite interlayer to form S intercalated graphite compounds, thus maximizing S loading and minimizing the dissolution of polysulfides. However, only a small amount of S can be intercalated into graphite even under the conditions of high pressure and/or high temperature due to small layer spacing (planar distance ≈0.34 nm).[26] Because of the large interlayer distance, expanded graphite has been investigated as host to embed S. The expanded graphite-embedded sulfur nanocomposites were normally synthesized by two-step reactions: thermal reduction of graphite oxides in H_2/Ar at a high temperature (450 °C) and flowed by S melt-diffusion at a low temperature of ≈155 °C.[27,28] Since S vapor can reduce graphite oxide (GO) at a high temperature, in this work we report a novel one-step method to synthesize S intercalated graphite by S in situ reducing GO and intercalating into the reduced graphite oxide (RGO) under vacuum at 600 °C. **Figure 1** schematically depicts the preparation process of the RGO/S composite. At room temperature, sulfur exists mainly in the form of cyclooctasulfur (S_8), as heating the mixture of graphite oxide and S_8 to 600 °C, the large molecule S_8 will be broken into smaller chain species S_2.[29,30] Due to the large interplanar distance of GO, these S_2 molecules can intercalate into GO to deoxygenate GO and form SO_2 gas.[31] Further S_2 intercalation into RGO will form S intercalated graphite compounds. By manipulating the interlayer distance of graphite oxide through controlling the degree of oxidation of graphite,[32] the S intercalation level can be maximized. However, the S_2 molecules deposited on the external surface and the edges of RGO interlayer may recombine to form cyclo-S_8 when the temperature is cooling down from 600 °C to room temperature. Due to the high solubility of CS_2 to S_8, the surface S_8 can be removed using CS_2 solvent at ease. Here, we demonstrate that the RGO/S composites with 52% S loading show high capacities and long cycling stabilities. The CS_2-wash treatment can further enhance the cycling stability of RGO/S composites. Almost no capacity decline can be observed for CS_2-washed RGO/S composites in 225 cycles.

Figure 2a shows the X-ray diffraction (XRD) patterns of pure S, pristine graphite, GO and RGO/S composite. The XRD pattern of S exhibits very sharp and strong peaks throughout the entire diffraction range, indicating a well-defined crystal S_8 structure. Graphite exhibits a sharp peak at $2\theta = 26.6°$ corresponding to the diffraction of (002) plane with interlayer distance of ≈0.34 nm.[33]

Dr. S. Zheng, Dr. Z. Han, Prof. J. Yang
School of Materials Science and Engineering
University of Shanghai for Science and Technology
Shanghai 200093, China
E-mail: jhyang@usst.edu.cn
Dr. Y. Wen, Dr. Y. Zhu, Dr. J. Wang, Prof. C. Wang
Department of Chemical and Biomolecular Engineering
University of Maryland
College Park, MD 20742, USA
E-mail: cswang@umd.edu
Dr. J. Wang
School of Materials Science and Engineering
Jiamusi University
Jiamusi 154007, China

DOI: 10.1002/aenm.201400482

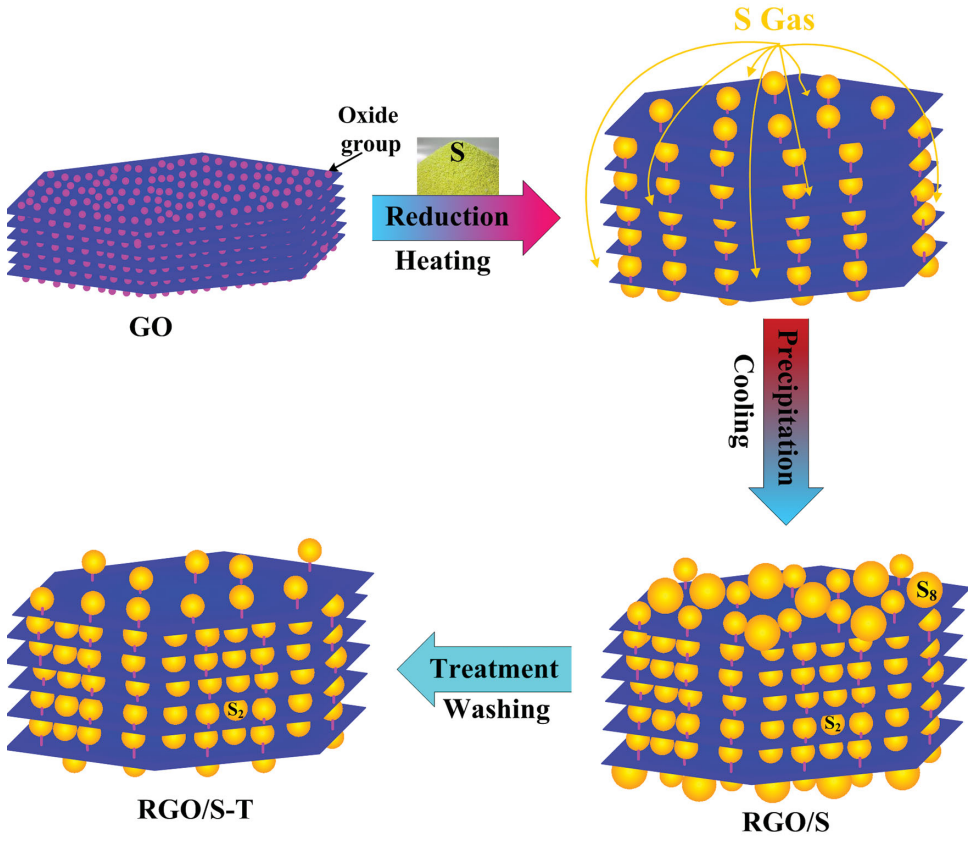

Figure 1. Schematic illustration of the preparation process of the RGO/S composite by in situ S reduction and intercalation method.

The GO shows a typical XRD pattern of graphite oxide with two peaks centered at 11 and 42 degrees, respectively. The diffraction peak of GO at ≈11 degree indicates that inter-planar distance is enlarged by oxygen functional groups. After S reduction and intercalation, the peak at 11 degree shifts to 25.4°, which is larger than diffraction peak 2θ (26.6°) of the pristine graphite. The diffraction peak at ≈25.4° for the RGO/S demonstrates that the as-prepared RGO/S composite has graphite-like structure but with larger interplanar distance than the pristine graphite. It has been reported that at 600 °C, the 99% of S_8 will be broken into S_2 and these S_2 can strongly interact with the surface of carbon to form a monolayered coverage of the carbon surface.[29,30] Due to its the high activity, S_2 can reduce the oxygen functional groups and simultaneously intercalate into the interlayers of expanded graphite to form RGO/S intercalated compounds. When the temperature is cooled down to the room temperature, the S_2 intercalated inside the RGO remains as the state of S_2, but the S_2 deposited on the external surface of RGO may change back to S_8.[30] The diffraction peaks of surface S_8 in RGO/S are visible but the intensities are significantly reduced, demonstrating small amount of crystal S_8 exists on the surface of the expanded graphite. The monolayer S_2 confined inside the interlayer spacing cannot be detected by XRD.

Raman spectroscopy is a powerful and widely used technique for characterization of the graphite and graphene.[34] The Raman spectra of GO and RGO/S are shown in Figure 2b. The Raman spectrum of a commercial graphene was also measured as a control. The Raman spectra of all three samples display two prominent peaks, which correspond to the well-documented G and D bands. The G band is usually assigned to the E_{2g} phonon of C sp^2 atoms, while the D band originates from a breathing κ-point phonon with A_{1g} symmetry and related to local defects and disorders.[35] The G band of GO is at 1599 cm^{-1}. After S reduction and intercalation, the G band of the RGO/S composite shift to 1596 cm^{-1}, which is more close to the G band (1594 cm^{-1}) of the commercial graphene, indicating that the graphite oxide was reduced into graphite by sulfur under vacuum at 600 °C, which is similar to classical thermal reduction of GO by H_2 or H_2/Ar gas at similar temperatures. The I_D/I_G ratio is increased from 0.92 for the GO to 1.08 for the RGO/S, but the ID/IG ratio of the RGO/S is still slightly smaller than that of the commercial graphene. The increases of the I_D/I_G ratios are associated with more local defects and disorders mainly arising from deoxygenation of the GO. Therefore, the in situ formed RGO/S (reduced graphite oxide/S) has fewer defects than commercial graphene made from reduction of GO using H_2. The RGO prepared by in situ S_2 reduction will be more conducive than commercial graphene, thus the in situ formed RGO/S composite will have better rate performance than G/S composites.

Fourier transform infrared (FTIR) was also employed to analyze GO and RGO/S samples, as shown in Figure 2c. The FTIR spectra of GO exhibit very sharp and strong peaks throughout the entire wave number range, located at 3332, 2108, 1724,

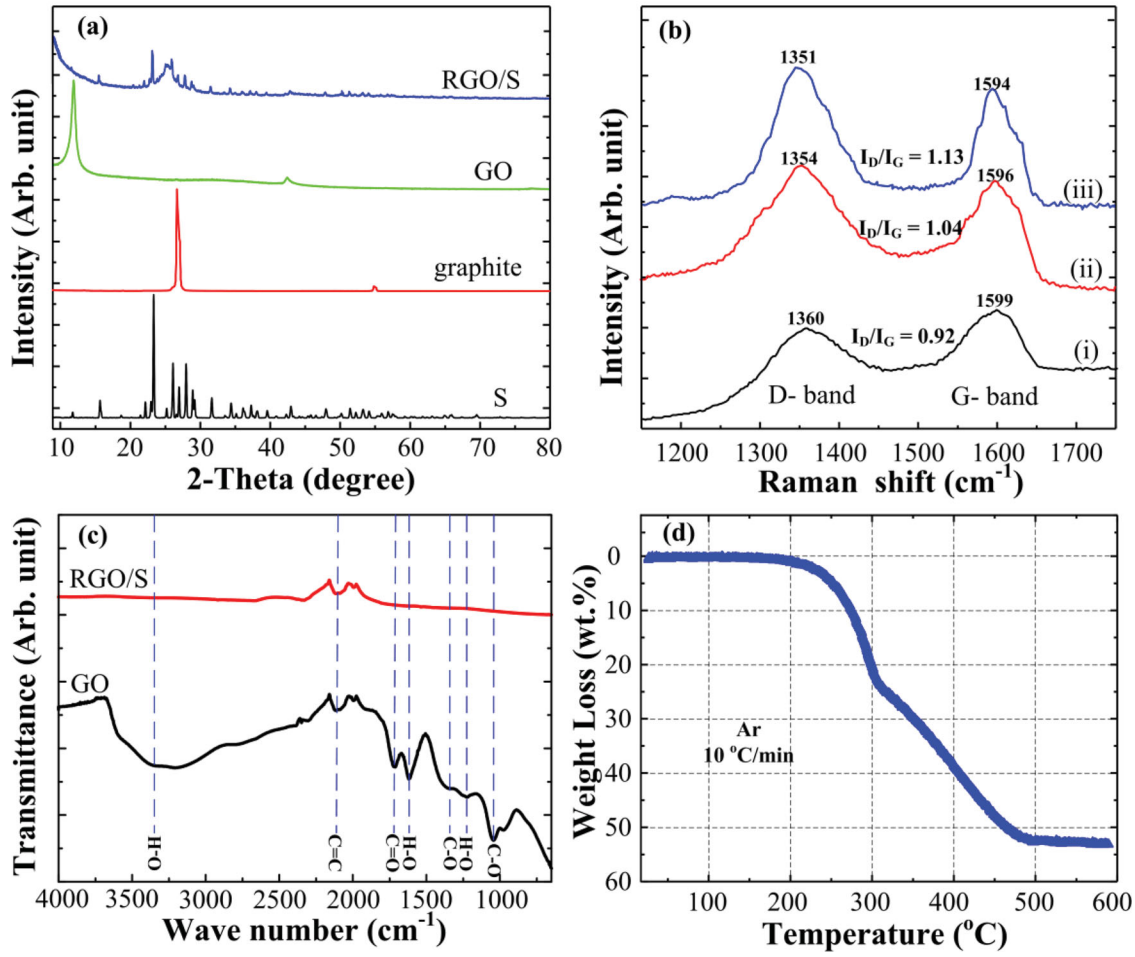

Figure 2. a) XRD patterns of pure S, graphite, GO and RGO/S and b) Raman spectra of samples: i) GO, ii) RGO/S composite, and iii) commercial graphene. c) FTIR spectra of GO and RGO/S and d) TGA profile of RGO/S composite.

1622, 1350, 1222 and 1045 cm^{-1}, which are due to the vibration and deformation bands of O–H and C=O stretching vibrations from carbonyl groups, C=C configurable vibrations from the aromatic zooms, C–OH stretching vibrations, C–O vibrations from epoxy groups and C–O vibrations from alkoxy groups, respectively.[36] However, all of the peaks related to the oxygen containing functional groups vanish in the FTIR spectrum of RGO/S composites, revealing that these oxygen-containing functional groups of the GO were almost completely removed in the preparation process of RGO/S composite, i.e., the GO can be reduced through our in situ sulfur reduction approach.

The S loading in RGO/S composite was measured using thermogravimetric analyzer (TGA). TGA profile of the RGO/S composite in Figure 2d reveals that an amount of 52% S is loaded into the RGO, which is slightly lower than its initial percentage of 67% in the starting materials. This difference demonstrates that some of S indeed involves in the reduction of GO, i.e., some S extracted as SO_2 by deoxygenation of GO into RGO. In addition, the TGA curve of the RGO/S composite shows two-step weight loss. In the first step, an onset weight loss takes place at around 180 °C with a loss of about 22% at 300 °C. The temperature range is identical to that of evaporation for the pristine S (see Supporting Information Figure S1), so this step corresponds to the evaporation of S_8 deposition on the surface of RGO. The second weight loss ranging from 300 to around 500 °C releases the rest of S (30%), which is associated with the extraction of intercalated S_2 in the interlayer of RGO. The amount is significantly higher than that of the reported graphite/S composite synthesized in high-pressure and/or high-temperature.[20] The increase of S loading can be attributed to larger inter-planar distance of RGO than that of the graphite. The two-step S releasing result is similar to behavior of the high temperature S incorporated into porous carbon.[14,18]

The morphologies of GO and RGO/S are presented in scanning electron microscopy (SEM) images in **Figure 3**. The GO has large, agglomerated graphite-like particles with a deeply connected lamellar morphology (Figure 3a). After deoxygenation of GO and S intercalation into the interlayer, the RGO maintains the graphite-like morphology of GO in the RGO/S composite (Figure 3b). The graphite-like morphology of the RGO/S is largely different from the previous reported graphene-like structure of the expanded graphite/S composite in ref. [27,28], which consists of connected graphene layer with very

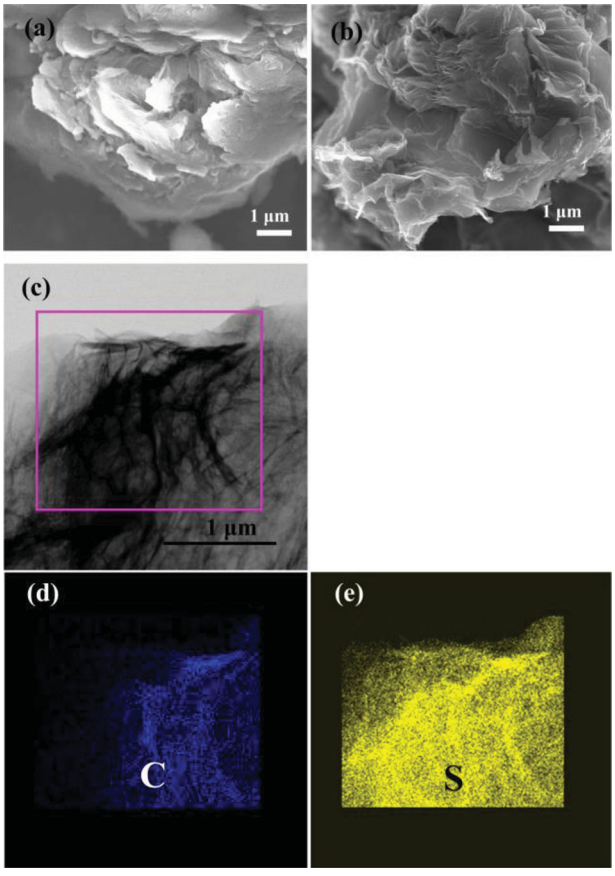

Figure 3. a) SEM image of GO, b) SEM image of RGO/S, c) HRTEM images of RGO/S, and d,e) the corresponding EDS maps of the C and S in image (c).

large and irregular interlayer distance. The graphite-like morphology of RGO/S with expanded interlayer can effectively protect S and formed polysulfides from dissolution into liquid electrolytes and also enhance the electronic conductivity. Moreover, no large S_8 particles aggregation can be found in the RGO/S composite, which suggests that the most S is well dispersed in the RGO, which is also confirmed by very weak S_8 XRD peaks in Figure 2a. The microstructures of the RGO/S were further characterized by high-resolution transmission electron microscopy (HRTEM) and elemental mappings presented in Figure 3c–e, illustrating a layer structure of RGO and uniform distribution of S in the RGO/S composite. No large bulk S aggregations can be found in the composite from the TEM image in Figure 3c. The dark ripples in the TEM images indicate that the RGO sheet has graphite layer structure, and thus favors to effectively immobilize S. The elemental concentration mappings of C and S of the area outlined by the purple frame in Figure 3c follows dark ripples further corroborate that the S_2 is mainly intercalate into the graphite interlayers in the RGO/S composite.

The first three lithiation/delithiation behaviors of the RGO/S electrodes using the electrolyte of 1.0 M LiTFSI in TEGDME were characterized by cyclic voltammetry (CV), as displayed in **Figure 4**a. Four peaks can be clearly observed in the first cathodic scan, i.e., two large peaks at around 2.4 and 2.0 V (vs Li/Li^+) together with two relatively weak peaks at about 2.1 and 1.8 V (vs Li/Li^+). The peak at around 2.4 V (vs Li/Li^+) is ascribed to the reduction of S (S_8) to soluble high-order Li polysulfides (Li_2S_8 and Li_2S_6). The peak of 2.1 V (vs Li/Li^+) probably corresponds to the transformation of the high-order lithium polysulfide into lower-order Li polysulfides. The peak at 2.0 V (vs Li/Li^+) is related to the conversion of low-order polysulfides and lithiation of intercalated S_2 (near to the surface of RGO) to insoluble Li_2S_2 and/or Li_2S. These peaks are consistent with the conventional redox reaction between S with Li during lithiation process as reported.[14,18,37] In addition to the conventional redox reaction peaks, a board peak positioned at around 1.8 V (starting at 1.9 V (vs Li/Li^+)) appears, and is attributed to lithiation of inner intercalated S_2 into Li_2S_2 and/or Li_2S. The low-voltage and broad peak is induced by the bonding between S_2 and RGO layer. Such a low-voltage peak was previously reported in both carbon-S composites and conductive polymer-S composites synthesized at relatively higher temperature (≥300 °C) and attributed to chemical interaction between S and carbon of matrix.[18,19,38] This result implies that inner S_2 is chemically bonded to atoms of the layer-structure RGO, which in turn explains why higher evaporating temperature of S were required in the TGA measurement (Figure 2d). In the anodic scan curve of the first cycle, one sharp oxidation peak at about 2.4 V (vs Li/Li^+) along with a shoulder peak at 2.5 V (vs Li/Li^+) can be observed that is attributed to the conversion of Li_2S and polysulfides into elemental S. As compared to the first cycle, the peak current of both the cathodic and the anodic peaks become slightly lower but show very stable in the following cycles, suggesting that the RGO/S can effectively accommodate the volume change during reversible electrochemical reaction and protect intercalated S_2 from dissolution. Figure 4b shows the initial three cycles' charge/discharge curves of the RGO/S in 1.0 M LiTFSI (TEGDME) at current density of 100 mA g^{-1}. The positions of the plateaus correspond well to the typical peaks in the CV curves. The lithiation capacity is around 1150 mAh g^{-1} in the first cycle, 1020 mAh g^{-1} in the second cycle and about 1000 mAh g^{-1} in the third cycle, showing high reversible capacities. Figure 4c represents the cycling performance and Coulombic efficiency for the RGO/S cathode in 1.0 M LiTFSI (TEGDME) at a current density of 100 mA g^{-1}. Similar to other carbon-S and graphene-S composite cathodes reported in literatures,[17,19,23,25] the capacity gradually decay in the first 60 cycles and then stabilize at a range of 630 to 680 mAh g^{-1}, which corresponds to 60% of initial capacity, i.e., a capacity retention ratio of 60%. The initial capacity decay is attributed to the dissolution of high-order polysulfides formed from S_8 that is coated on the outside surface of RGO particles. The 60% of capacity retention ratio is very close to the mass ratio of intercalated S in the interlayers to the total S content that was determined from the weight loss in the 300–500 °C range (second step) dividing by total weight loss in 200–500 °C (30:52) in the TGA test (Figure 2d). It can be deduced that the S intercalated in the RGO is responsible to these stable reversible capacities since the S_8 deposited on the external surface of RGO would totally dissolve into electrolyte during initial 60 cycles. Therefore, one-step synthesized RGO/S under vacuum at 600 °C can effectively stabilize the intercalated S_2. To further support this point, a conventional carbonate-based electrolyte (1.0 M $LiPF_6$ in a mixture of

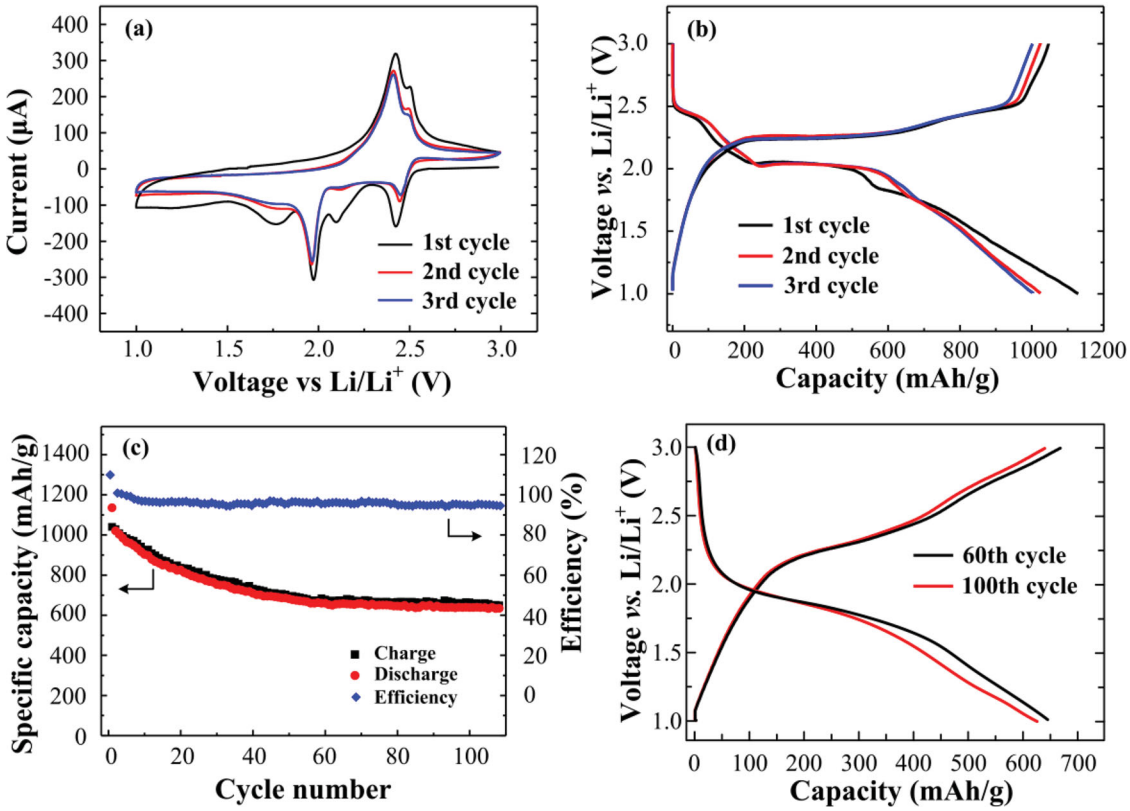

Figure 4. a) Cyclic voltammograms of the RGO/S composite electrode in the first three cycles within the voltage window of 1.0–3.0 V at a scan rate of 0.1 mV s^{-1}. b) Discharge/charge voltage profiles of the RGO/S electrode in the first three cycles at a current density of 100 mA g^{-1}. c) Cycling performance and Coulombic efficiency of the RGO/S cathode at 100 mA g^{-1}. d) Discharge-charge curves of the RGO/S electrode in the 60th and 100th cycle at a current density of 100 mA g^{-1} using the electrolyte of 1.0 M LiTFSI in TEGDME.

ethylene carbonate/diethyl carbonate (EC/DEC, 1:1 by volume)), which is incompatible with the natural state S_8 cathode due to reaction between polysulfide anions and carbonate solvent,[39,40] was used to test the stability of intercalated S_2 in the RGO. The RGO/S cathode in 1.0 M $LiPF_6$ (EC/DEC 1:1 v/v) delivers a discharge capacity of around 1000 mAh g^{-1} in the first cycle, but the capacity drops quickly to approximately 465 mAh g^{-1} in the second cycle, and then the capacities stabilize at around 450 mAh g^{-1} for prolonged cycles (see Supporting Information Figure S2). The voltage plateau at 2.5 V (vs Li/Li^+) observed in the first lithiation disappears in the following discharge cycles, confirming the reaction of dissolved polysulfides with carbonate electrolyte. The discharge curve after the first cycle shows only a slope potential plateau at 1.8 V (vs Li/Li^+), representing the lithiation of the intercalated S_2, that is, the S (S_8) deposited on the external surface of RGO is easily dissolved into the carbonate-based electrolyte and/or reacted with carbonate solvent but the intercalated S_2 in the interlayer of graphite is stable due to both physical confinement and chemical interaction. The S_2 intercalated graphite cathodes allow using cheap carbonate-based electrolyte if the S_8 on the external surface of GO can be removed. In addition to high capacity retention, the RGO/S composite cathode also has an average Coulombic efficiency of around 98%, indicating reliable stability. As shown in Figure 4d, the similarity of discharge/charge curves of the RGO/S cathode in the1.0 M LiTFSI (TEGDME) during 60 and 100 cycles demonstrates a highly stable and reversible charge/discharge behavior of intercalated S_2 during cycles. After 60 charge/discharge cycles, the voltage plateau of 2.5 V (vs Li/Li^+) presented in the initial cycles (see Figure 4b) completely disappears, which further verifying the intercalated S_2 in the interlayer of graphite is effectively immobilized.

The rate capability behaviors of the RGO/S composite electrode in 1.0 M LiTFSI (TEGDME) at different current density from 0.1 to 15.0 A g^{-1} are shown in **Figure 5**a. A reversible capacity of around 500 mAh g^{-1} can be obtained at a high current density of 1.0 A g^{-1}, owing to the good electrical conductivity of RGO matrix and the uniformly dispersed S. The value is about 350 mAh g^{-1} for 2.0 A g^{-1} and 280 mAh g^{-1} for 4.0 A g^{-1}. A capacity of more than 100 mAh g^{-1} can still be delivered even when the current density increases to 15.0 A g^{-1}. Moreover, the capacity of approximately 600 mAh g^{-1} can be retained when the current density is returned from 15.0 to 0.1 A g^{-1}, showing a great merit for an abuse tolerance of Li-S battery with varied current densities. To get further insight into the kinetics evolution during charge/discharge cycles, electrochemical impedance spectra (EIS) of the RGO/S composite cathode using the electrolyte of 1.0 M LiTFSI (TEGDME) in the 1st and 100th cycles at the fully charged states were measured and are compared in Figure 5b. The EIS spectra are consists of overlapped two semicircles at high frequencies an inclined line in low frequency regions. The first high-frequency semicircles are attributed

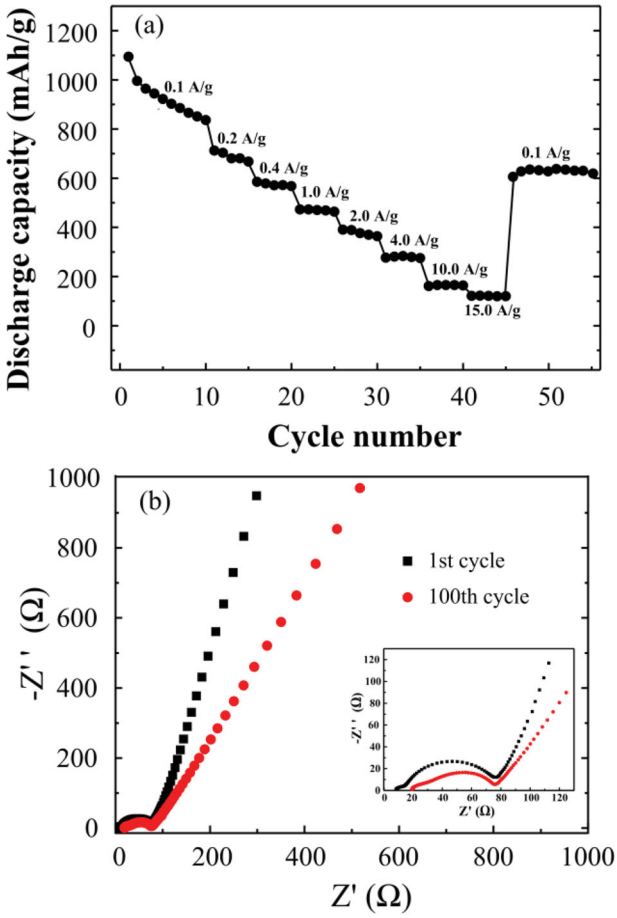

Figure 5. a) Rate capability behaviors of the RGO/S composite electrode at current density from 0.1 A g^{-1} to 15.0 A g^{-1} and b) EIS spectra of the RGO/S composite cathode in the 1st and 100th cycles (insert is the enlarged EIS plot in high-frequency region) using the electrolyte of 1.0 M LiTFSI in TEGDME.

to insulating layer of lithium sulfide and SEI on Li anode and the second semicircle is mainly due to charge-transfer of RGO/S cathode. The inclined line in low frequency regions is due to the ion diffusion in the RGO/S cathode. It is obvious that the RGO/S composite electrode exhibits a stable charge-transfer resistance upon cycling, which could be attributed to the good conductivity and the stable structure of the RGO/S composite.

Since the intercalated S_2 in the interlayer of RGO can directly convert to insoluble Li_2S_2 and/or Li_2S, while the surface S_8 will be dissolved into electrolytes through formation soluble high-order polysufides during lithiation/delithiation. The dissolution of the S_8 results in low Coulombic efficiency and capacity decay, while the intercalated S_2 in expanded graphite interlayer maintains the reversible capacity, even enables to use cheap carbonate electrolytes in Li-S battery. If the surface S_8 can be removed, the S_2 intercalated expanded graphite composite cathode should have high Coulombic efficiency and long cycling life. Due to the high solubility of CS_2 to S_8, the RGO/S composite was washed using CS_2 to completely remove the surface S_8. The CS_2-washed RGO/S is denoted as RGO/S-T. The phase components of the RGO/S-T composite were characterized by XRD,

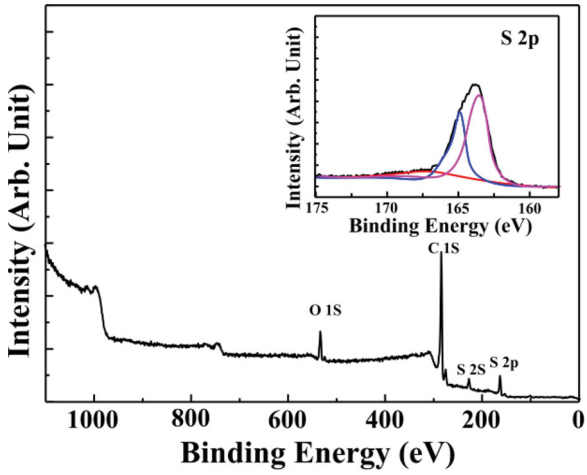

Figure 6. XPS spectra of RGO/S-T composite, with the inset showing the magnified S 2p spectrum.

as shown in Supporting Information Figure S3. As expected, the peaks belonging to S_8 crystalline phases disappear in the RGO/S-T sample. The difference in XRD pattern between the RGO/S (see Figure 2a) and the RGO/S-T suggests that the S_8 was removed by CS_2. Additionally, the almost disappearance of the weight loss of RGO/S-T at temperatures of 200–300 °C in TGA (Supporting Information Figure S4) also confirms that surface S_8 was removed by CS_2 washing, and only the 32% of S_2 is extracted from the interlayer of RGO in temperature range of 300–500 °C, which is consistent with the TGA curves of the RGO/S in Figure 2d. Therefore, The CS_2 only removes the surface S_8, but the intercalated S_2 is stable. The RGO/S-T composite material was also analyzed using X-ray photoelectron spectroscopy (XPS) techniques. **Figure 6** presents the survey scan and S 2p binding energy spectra of the RGO/S-T sample. The S 2p exhibits one strong peak at about 164.0 eV along with a broad weak peak centered at 167.0 eV. Further fitting indicates that the strong peak can be split into two peaks for 165.0 and 163.9 eV, respectively, which are assigned to S 2p1/2 and 2p3/2 due to spin orbit coupling, but the binding energies are slightly higher than those of the characteristic peaks of elemental S, which is mainly related to the signals come from the S confined in the RGO.[41,42] In addition, there exists a broad high binding energy peak positioned between 162 and 172 eV, which is an evidence of the strong interaction of sulfur and carbon.[43] The XPS result verifies that intercalated S_2 is immobilized by both physical confine and chemical interaction in the RGO.

The electrochemical performances of the RGO/S-T composite were also evaluated as cathodes for Li-S batteries in coin cells. The first three charge/discharge profiles of the RGO/S-T electrode using the electrolyte of 1.0 M LiTFSI in TEGDME at 100 mA g^{-1} are displayed in **Figure 7**a. The RGO/S-T can provide a capacity of around 870 mAh g^{-1} in the first cycle, 890 mAh g^{-1} in the second cycle, and approximately 905 mAh g^{-1} in the third cycle for the C/S-50-T cathode, showing remarkably high reversible capacity. The similar phenomena of capacity drop and recover during initial several charge/discharge cycles were also reported for the study of graphene-62.5% S composite cathode by Sun and co-workers and bulk mesoporous carbon-50% S

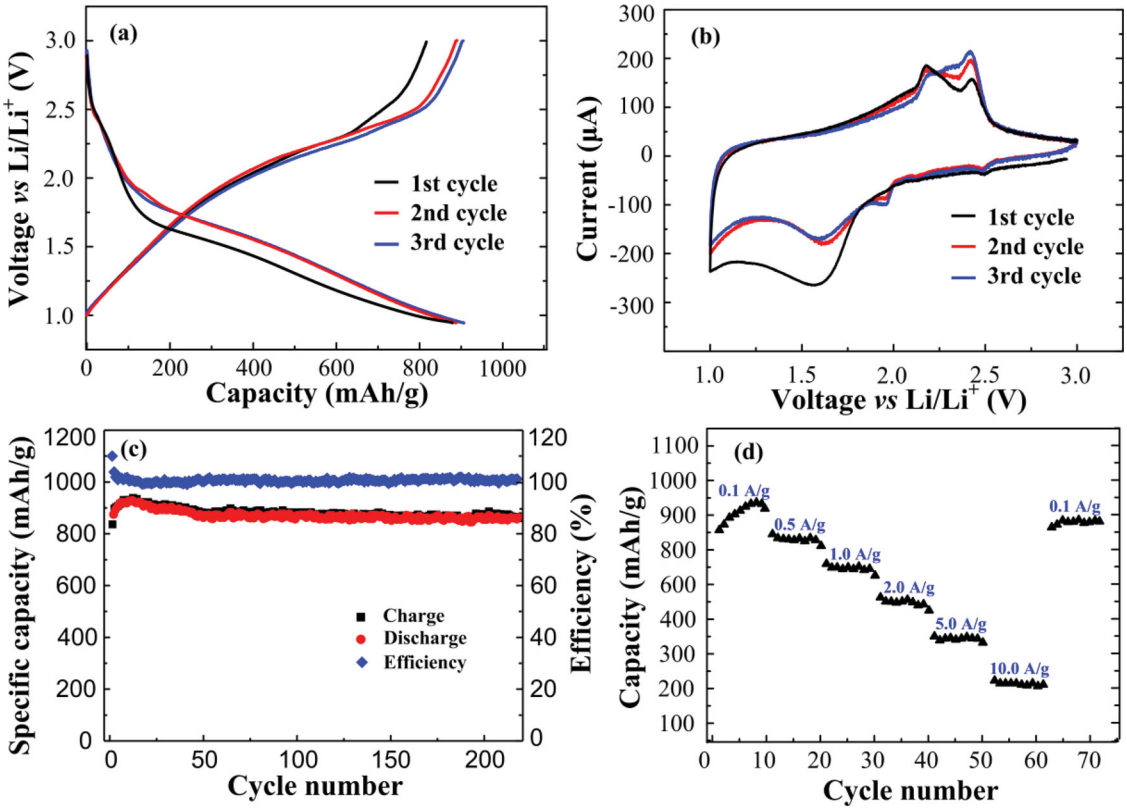

Figure 7. a) Discharge/charge voltage profiles of the RGO/S-T electrode in the first three cycles at a current density of 100 mA g^{-1}. b) Cyclic voltammograms of the RGO/S-T composite electrode in the first three cycles within the voltage window of 1.0–3.0 V at a scan rate of 0.1 mV s^{-1}. c) Cycling performance and Coulombic efficiency of the RGO/S-T cathode at 100 mA g^{-1}. d) Rate capability behaviors of the RGO/S-T composite electrode at current density from 0.1 A g^{-1} to 10.0 A g^{-1} using the electrolyte of 1.0 M LiTFSI in TEGDME.

cathode by Nazar's group.[17,44] This is probably related to an initial activation process. The mechanism will be explored in our following studies. The almost disappearance of plateau at 2.4–2.5 V (vs Li/Li^+) related to the lithiation of S_8 to soluble high-order Li polysulfides confirms that the surface S_8 was removed. The one long and slope plateau at 1.6–1.9 V (vs Li/Li^+) is attributed to lithiation of intercalated S_2 into low-order lithium polysulfides. CV curves of the RGO/S-T electrode consist of two main peaks at 1.9 and 1.7 V (vs Li/Li^+) in the first cathodic scan (see Figure 7b). Compared to the CV curves of RGO/S electrode (Figure 4a), peaks at ≈2.4 V (vs Li/Li^+) greatly shrink to almost invisible. After the first cycle, the low-voltage peak current near 1.7 V (vs Li/Li^+) was reduced and shifted toward more positive direction due to the size expansion of carbon matrix in the first lithiation. The anodic scan in CV curves shows two conjoint peaks between 2.1 and 2.5 V (vs Li/Li^+) due to the conversion of low-order polysulfides into elemental S. The stable cathodic and anodic current peaks in the first and following scans also demonstrate good cycling stability of the RGO/S-T composite cathode. The cycling performance of the RGO/S-T electrode is presented in Figure 7c, showing high Coulombic efficiency and long cycling stability. Even cycling up to more than 220 cycles, the RGO/S-T cathode retains a capacity of around 880 mAh g^{-1} and the Coulombic efficiency is close to 100% except for the initial few cycles. The cycling test of the Li-S cell is still under way. The long cycling stability and high Coulombic efficiency of the RGO/S-T cathodes in Li-S cell is attributed to the elimination of high-order polysulfide intermediates, thus avoiding the shuttle reaction. This fully proves that RGO/S composite synthesized using in situ one-step S reduction and intercalation strategy can greatly improve S utilization and stabilize the capacity during charge/discharge cycles. The rate capability behaviors of the RGO/S-T composite electrode in Li-S cell at different current density from 0.1 to 10.0 A g^{-1} are shown in Figure 7d. A reversible capacity of 700 mAh g^{-1} can be obtained at a high current density of 1.0 A g^{-1}. The value is about 500 mAh g^{-1} for 2.0 A g^{-1} and 300 mAh g^{-1} for 5.0 A g^{-1}. A capacity of more than 220 mAh g^{-1} can still be delivered even when the current density increases to 10.0 A g^{-1}. Moreover, the capacity of approximately 850 mAh g^{-1} can be retained when the current density is returned from 10.0 to 0.1 A g^{-1}. Obviously, the RGO/S-T cathode demonstrates an outstanding rate capability and a great merit for an abuse tolerance with varied current densities in Li-S battery, which is owing to the good electrical conductivity of RGO as matrix to support and connect with the highly dispersed S through both physical confine and chemical interaction.

In summary, the RGO/S composite synthesized via our in situ one-step S reduction and intercalation strategy shows high and stable capacities and good rate capability, in particular, after removing the surface S_8, RGO/S-T exhibits exceptional cycling stability and high rate performance. The superior electrochemical properties of the RGO/S cathode in Li-S

batteries is attributed to: i) a double role of S vapor in the high-temperature of 600 °C: assisted-reduction of GO into RGO and in situ intercalation into interlayer of RGO and bonding to interlayers, that is, the intercalated S_2 is immobilized by both physical confine and chemical interaction in the RGO, effectively stabilizing S_2; and ii) outstanding electrical and mechanical properties of layers structure of the RGO matrix which can not only significantly improve the conductivity of the S_2 but also effectively buffer the structural strain/stress caused by the large volume change during lithiation/delithiation. The unique properties of the RGO/S composite plus their simple fabrication make this class of materials attractive for further investigation for Li-S batteries applications.

Experimental Section

Synthesis of Graphite Oxide (GO): Graphite oxide was prepared using a modified Hummers method.[32] Firstly, 10 g of Johnson Matthey graphite powder (Aka regular graphite powder) and 5 g of $NaNO_3$ were placed in a three-necked flask with a stirrer chip. Then 230 mL of concentrated sulfuric acid was slowly added. The mixture was stirred in an ice water bath environment for about 2 h followed by gradually adding 30 g $KMnO_4$ (purity 99%) over about 2 h under slow stirring conditions, then heated up to 35 °C. Afterwards, 460 mL deionized (DI) water was added over the course of about 30 min with stirring. The resultant mixture was further stirred for 2 h followed by adding 200 mL of 30 % H_2O_2 aqueous solution and stirred for another 2 h. This suspension was then filtered and washed with DI water several times. Finally, the resulting brown filter cake was dried at 100 °C under vacuum for 24 h.

Preparation of RGO/S Composite: The prepared GO and the sublimed sulfur (Sigma-Aldrich) with a mass ratio of m_{GO}:m_S = 1:2 were mixed by ground milling. The mixture was sealed in an evacuated quartz tube, heated up to 600 °C at a rate of 5 °C min^{-1}, and then maintain at this temperature for 6 h; followed by a slow cooling rate of 0.5 °C min^{-1} time to room temperature to ensure a complete infiltration of sulfur into the layers of RGO. The as-prepared RGO/S composite was treated with CS_2 for no less than three times, and the resulting sample was dried in vacuum oven at 100 °C for 2 h, indicated as RGO/S-T. The actual sulfur content in the composite was measured using TGA on a Netzsch STA 449 F1, Germany, with a heating rate of 10 °C min^{-1}, and high purity Ar as the purge gas.

Structural Characterization: XRD patterns of samples were recorded in the 2-theta range from 10–80° using Rigaku D/max 2400, Japan with Cu Kα radiation. Raman spectra were scanned from 2850 to 100 cm^{-1} on a high resolution dispersive Raman spectroscopic microscope (Horiba Jobin Yvon, USA). Raman spectra of a commercial graphene purchased from Graphene Supermarket, USA, was also measured as the reference. FTIR spectra were recorded on a Bruker VECTOR 22 spectrometer in the frequency range of 4000–500 cm^{-1}. XPS was carried out on a RBD upgraded PHI-5000C ESCA system (Perkin Elmer) with Mg Kα radiation (1253.6 eV). SEM images equipped with an energy dispersive X-ray spectrometry (EDS) were used to characterize the RGO/S composite using a Hitachi S-4700, Japan. The TEM samples were examined in a JEM 3010 microscope. High spatial resolution imaging and microanalysis were performed with an FEI Titan 80-300 analytical scanning transmission electron microscope (STEM) operated at 300 kV accelerating voltage and equipped with a Fischione Instruments model 3000 high-angle annular dark-field (HAADF) detector and an EDAX lithium-drifted silicon X-ray energy-dispersive spectrometer (XEDS).

Electrochemical Measurements: The electrode slurry were prepared by mixing S-containing composite with carbon black and sodium carboxymethyl cellulose (CMC) binder at the weight ratio of 80:10:10. The film electrode was prepared by casting the slurry onto aluminum foil using a doctor blade and dried at 60 °C overnight in a vacuum oven. The active material loading was around 1 mg/cm^2. The coin cells were assembled in a glove box filled with high pure Ar. Lithium metal was used as the counter electrode and reference electrode. The separator was microporous polypropylene Celgard3501 (Celgard, LLC Corp., USA). The electrolyte was 1.0 M bis- (trifluoromethane)sulfonimide lithium salt (LiTFSI, Sigma-Aldrich) in tetra(ethylene glycol)dimethyl ether (TEGDME, Sigma-Aldrich). The charge and discharge performances of the coin cells were tested in a potential range between 1.0 and 3.0 V at ambient temperature using Arbin battery test station (BT2000, Arbin Instruments, USA) The specific capacity was calculated on the basis of the active sulfur material obtained from TGA measurement. The electrode reaction kinetics of electrodes were measured using EIS in the frequency ranges from 100 kHz to 10 mHz (Solatron 1260/1287 Electrochemical Interface; Solatron Metrology, UK). The cyclic voltammetry (CV) measurement was conducted using a Gamry Reference 3000 (Gamry Co., USA) at a scan rate of 0.1 mV s^{-1}.

Supporting Information

Supporting Information is available from the Wiley Online Library or from the author.

Acknowledgements

The authors gratefully acknowledge the support of the Nanostructures for Electrical Energy Storage (NEES), an Energy Frontier Research Center funded by the U.S. Department of Energy, Office of Science, Office of Basic Energy Sciences under Award Number DESC0001160. They also acknowledge the support of the Maryland NanoCenter and its NispLab. The NispLab is supported in part by the NSF as a MRSEC Shared Experimental Facility. This work was also supported by the National Science Foundation of China (No. 51272157).

Received: March 19, 2014
Revised: June 4, 2014
Published online: June 30, 2014

[1] D. Herbert, J. Ulam, *U.S. Pat.*, 3,043,896, **1962**.
[2] E. Peled, A. Gorenshtein, M. Segal, Y. Sternberg, *J. Power Sources* **1989**, *26*, 269.
[3] X. Ji, L. F. Nazar, *J. Mater. Chem.* **2010**, *20*, 9821.
[4] V. S. Kolosnitsyn, E. V. Karaseva, *Russ. J. Electrochem.* **2008**, *44*, 506.
[5] Y. Zhang, Y. Zhao, K. Sun, P. Chen, *Open Mater. Sci. J.* **2011**, *5*, 215.
[6] P. G. Bruce, S. A. Freunberger, L. J. Hardwick, J.-M. Tarascon, *Nat. Mater.* **2012**, *11*, 19.
[7] B. Scrosati, J. Hassoun, Y. K. Sun, *Energy Environ. Sci.* **2011**, *4*, 3287.
[8] Y. Yang, G. Zheng, Y. Cui, *Chem. Soc. Rev.* **2013**, *42*, 3018.
[9] L. Suo, Y. Hu, H. Li, M. Armand, L. Chen, *Nat. Commun.* **2013**, *4*, 1481.
[10] J. Wang, J. Yang, J. Xie, N. Xu, *Adv. Mater.* **2002**, *14*, 963.
[11] W. Zheng, Y. Liu, X. Hu, C. Zhang, *Electrochim. Acta* **2006**, *51*, 1330.
[12] E. S. Shin, K. Kim, S. H. Oh, W. Cho, *Chem. Commun.* **2013**, *49*, 2004.
[13] S. Xin, L. Gu, N. Zhao, Y. Yin, L. Zhou, Y. Guo, L. Wang, *J. Am. Chem. Soc.* **2012**, *134*, 18510.
[14] X. Ji, K. T. Lee, L. F. Nazar, *Nat. Mater.* **2009**, *8*, 500.
[15] G. Zhou, D. Wang, F. Li, P. Hou, L. Yin, C. Liu, G. Lu, I. R. Gentle, H. Cheng, *Energy Environ. Sci.* **2012**, *5*, 8901.
[16] S. Zheng, Y. Chen, Y. Xu, F. Yi, Y. Zhu, Y. Liu, J. Yang, C. Wang, *ACS Nano* **2013**, *7*, 10995.

[17] J. Schuster, G. He, B. Mandlmeier, T. Yim, K. T. Lee, T. Bein, L. F. Nazar, *Angew. Chem. Int. Ed.* **2012**, *51*, 3591.
[18] J. Guo, Y. Xu, C. Wang, *Nano Lett.* **2011**, *11*, 4288.
[19] B. Zhang, X. Qin, G. Li, X. Gao, *Energy Environ. Sci.* **2010**, *3*, 1531.
[20] K. S. Novoselov, A. K. Geim, S. V. Morozov, D. Jiang, M. I. Katsnelson, I. V. Grigorieva, S. V. Dubonos, A. A. Firsov, *Nature* **2005**, *438*, 197.
[21] C. Gmez-Navarro, R. T. Weitz, A. M. Bittner, M. Scolari, A. Mews, M. Burghard, K. Fern, *Nano Lett.* **2007**, *7*, 3499.
[22] H. Chen, M. B. Muller, K. J. Gilmore, G. G. Wallace, D. Li, *Adv. Mater.* **2008**, *20*, 3557.
[23] H. Wang, Y. Yang, Y. Liang, J. T. Robinson, Y. Li, A. Jackson, Y. Cui, H. Dai, *Nano Lett.* **2011**, *11*, 2644.
[24] T. Lin, Y. Tang, H. Bi, Z. Liu, F. Huang, X. Xie, M. Jiang, *Energy Environ. Sci.* **2013**, *6*, 1283.
[25] L. Ji, M. Rao, H. Zheng, L. Zhang, Y. Li, W. Duan, J. Guo, E. J. Cairns, Y. Zhang, *J. Am. Chem. Soc.* **2011**, *133*, 18522.
[26] R. Ricardo da Silva, J. H. S. Torres, Y. Kopelevich, *Phys. Rev. Lett.* **2001**, *87*, 147001.
[27] S. Li, M. Xie, J. B. Liu, H. Wang, H. Yan. *Electrochem. Solid State Lett.* **2011**, *14*, A105.
[28] Y. Wang, L. Huang, L. Sun, S. Xie, G. Xu, S. Chen, Y. Xu, J. Li, S. Chou, S. Dou, S. Sun, *J. Mater. Chem.* **2012**, *22*, 4744.
[29] V. V. Shinkarev, V. B. Fenelonov, G. G. Kuvshinov, *Carbon* **2003**, *41*, 295.
[30] B. Meyer, *Chem. Rev.* **1976**, *76*, 367.
[31] H. Poh, P. Simek, Z. Sofer, M. Pumera, *ACS Nano* **2013**, *7*, 5262.
[32] W. S. Hummers, R. E. Offeman, *J. Am. Chem. Soc.* **1958**, *80*, 1339.
[33] Y. Qian, A. Vu, W. Smyrl, A. Stein, *J. Electrochem. Soc.* **2012**, *159*, A1135.
[34] S. H. Huh, in Thermal Reduction of Graphene Oxide, Physics and Applications of Graphene-Experiments (Ed: S. Mikhailov), InTech, Rijeka **2011**.
[35] A. Ferrari, J. Meyer, V. Scardaci, C. Casiraghi, M. Lazzeri, F. Mauri, S. Piscanec, D. Jiang, K. S. Novoselov, S. Roth, A. K. Geim, *Phys. Rev. Lett.* **2006**, *97*, 187401.
[36] A. V. Murugan, T. Muraliganth, A. Manthiram, *Chem. Mater.* **2009**, *21*, 5004.
[37] C. Barchasz, F. Molton, C. Duboc, J. Lepretre, S. Patoux, F. Alloin, *Anal. Chem.* **2012**, *84*, 3973.
[38] J. Wang, J. Yang, C. Wan, K. Du, J. Xie, N. Xu, *Adv. Funct. Mater.* **2003**, *13*, 487.
[39] S. S. Zhang, *Energies* **2012**, *5*, 5190.
[40] J. Gao, M. A. Lowe, Y. Kiya, H. D. Abruna, *J. Phys. Chem. C* **2011**, *115*, 25132.
[41] V. Toniazzo, C. Mustin, J. Portal, B. Humbert, R. Benoit, R. Erre, *Appl. Surf. Sci.* **1999**, *143*, 229.
[42] G. Greczynski, Th. Kugler, W. Salaneck, *Thin Solid Film* **1999**, *354*, 129.
[43] Y. Yang, G. Yu, J. Chu, H. Wu, M. Vosgueritchian, Y. Yao, Z. Bao, Y. Cui, *ACS Nano* **2011**, *5*, 9187.
[44] H. Sun, G. Xu, Y. Xu, S. Sun, X. Zhang, Y. Qiu, S. Yang, *Nano Res.* **2012**, *5*, 726.

